This is a repository copy of *Self-consistent scattering model of carrier dynamics in GaAs-AlGaAs terahertz quantum-cascade lasers* .

White Rose Research Online URL for this paper:
http://eprints.whiterose.ac.uk/713/

Article:

Self-Consistent Scattering Model of Carrier Dynamics in GaAs–AlGaAs Terahertz Quantum-Cascade Lasers

D. Indjin, P. Harrison, *Senior Member, IEEE*, R. W. Kelsall, and Z. Ikonić

Abstract—Intersubband electron scattering transport in terahertz GaAs–AlGaAs quantum cascade lasers is analyzed, using a full 13-level self-consistent rate equation model. The approach includes all relevant scattering mechanisms between injector–collector and active region states in the cascade structures. Employing an energy balance equation which includes the influence of both electron longitudinal optical phonon and electron–electron scattering, the method also enables evaluation of the average electron temperature of the nonequilibrium carrier distributions in the device. The electron temperature is found to give a strong influence on the output characteristics, particularly at very low temperatures. The threshold currents and electric field-current density characteristics are in very good agreement with experiment, implying that the model has a strong predictive capability.

Index Terms—Electron temperature, intersubband transitions, quantum-cascade lasers, terahertz.

Fig. 1. A schematic diagram of quasi-bound energy levels and associated wave functions squared for $1(1/2)$ periods of a GaAs–Al$_{0.15}$Ga$_{0.85}$As terahertz QCL: injector (levels 8, 10, 11 and 13) active region (3, 5, 7, 9 and 12) collector (1, 2, 4 and 6). The layer sequence of one period of the structure, in nanometers, from left to right starting from the injection barrier is **4.3**, 18.8, **0.8**, 15.8, **0.6**, 11.7, **2.5**, 10.3, **2.9**, 10.2, **3.0**, 10.8, **3.3**, 9.9, ([14]). The normal script denotes the wells, bold script the barriers, and underscore the doped region, with a nominal donor sheet density $N_s = 4.08 \times 10^{10}$ cm^{-2} per period.

T HE QUANTUM-cascade laser (QCL), since its first realization [1], has demonstrated an impressive extension of the mid-infrared frequency range [2]–[5] and until recently could be operated at wavelengths as long as 24 μm [6]–[8]. This has stimulated a number of experimental [9], [10] and theoretical [11] studies of QCL structures designed for emission at terahertz frequencies well below the forbidden phonon Reststrahlenband. Considerable research effort has recently resulted in theoretical prediction of population inversion by Monte Carlo studies [12], followed by luminescence measurements [13], and finally the laser action [14] at $\lambda \sim 69$ μm (4.4 THz) in a GaAs–AlGaAs QCL. Most recently, lasing at $\lambda \sim 66$ μm has been demonstrated in similar structures with very low waveguide losses [15].

Successful experimental developments have stimulated further interest in theoretical work in order to indicate routes to optimized layer design for improved output characteristics, particularly at higher working temperatures. The charge transport in QCLs is due mainly to incoherent-scattering mechanisms [16], and all principal electron longitudinal optical (LO) phonon and electron–electron scattering mechanisms have to be included [17], [18]. This applies not only to the active region, where laser emission takes place, but also to the injector–collector region. The analysis of the operating characteristics of terahertz QCLs is more complex, i.e., computationally demanding, than for mid-infrared devices. This is because the energy separation between most of subbands is smaller than the LO phonon
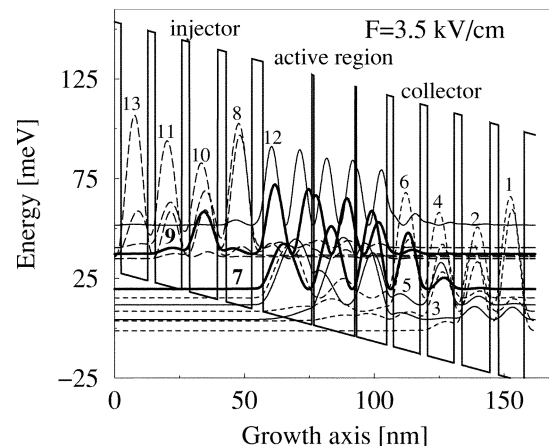
energy and electron–electron scattering becomes the dominant scattering mechanism [9], hence necessitating a large number of possibly relevant scattering processes to be accounted for. Additionally, the electron temperature is expected to exceed significantly the lattice temperature. In this letter, two main topics are addressed: 1) development of a technique to analyze terahertz QCLs as an alternative to the full microscopic, but computationally more demanding, Monte Carlo method [12], [16]; 2) extraction of the QCL output characteristics and exploration of the influence of electron temperature thereon.

The electronic structure of a terahertz QCL [14] is illustrated in Fig. 1. Radiative transitions occur between states 9 and 7, while levels 3, 5, and 12 are the ground, the first excited and higher states of the active region, respectively. Simulating electron flow in a cascade requires one to have scattering rates for all intra- and inter-period processes, and an assumption is made that each period of the cascade behaves in the same manner (periodic boundary conditions). Calculation of all these scattering rates formally necessitates for energy states/wavefunctions in two full periods, but in view of negligible active-to-active region coupling, $1(1/2)$ period (Fig. 1) suffices. Periodic boundary conditions imply that the wavefunctions in the two injector are shifted in space and energy versions of each other, though we have checked that using explicitly evaluated wave functions for the structure in Fig. 1 with hard boundary conditions gives a negligible difference in device output character-

istics (less than 3%). To implement periodic boundary conditions, the rate equations were written so that carriers were cycled around the 13-level system, i.e., electrons scattering outside the considered period reappear in equivalent states inside. Electron–electron scattering is calculated using Fermi golden rule within static screening approximation. The k-space averaging is done assuming Fermi–Dirac distribution within each subband individually, with common value of electron temperature in all subbands. All processes which, compared with electron-LO phonon scattering, make a nonnegligible contribution to the transport ($\sim$400) are included: the accuracy of this approximation has been confirmed in one-off calculation in which every electron–electron process ($\sim$8000) was considered. The steady state subband populations of the active region are written as

$$n_i = \left[\sum_{j=1, j\neq i}^{13} \frac{n_j}{\tau_{ji}} \right] \left[\sum_{j=1, j\neq i}^{13} \frac{1}{\tau_{ij}} \right]^{-1} \qquad (1)$$

where $i = 3, 5, 7, 9,$ and 12. The population of the ground collector level 1 is written as

$$n_1 = \left[\sum_k \frac{n_k}{\tau_{k1}} + \sum_s \frac{n_s}{\tau_{s8}} \right] \left[\sum_k \frac{1}{\tau_{1k}} + \sum_s \frac{1}{\tau_{8s}} \right]^{-1} \qquad (2)$$

where $k = 2, \ldots, 7, 9, 12$ and $s = 3, 5, 7, 9, 12$, and similarly for other injector and collector states. The scattering time τ_{if} is a function of both n_i and n_f, the initial and final subband populations. Hence, this set of equations has to be solved self-consistently using an iterative procedure [11], [19], [20].

At equilibrium, the rate at which the electron distributions gain kinetic energy (relative to the particular subband minimum) through scattering, will balance with the rate at which they lose kinetic energy to the lattice. Despite the fact that electron–electron scattering is elastic as far as total energy is concerned, intersubband electron–electron transitions do convert potential energy into kinetic energy (or vice-versa). This work this would lead to an increase (decrease) in the total kinetic energy of a subband population, because the potential energy as defined here includes the quantised component of the kinetic energy. Hence, the kinetic energy balance condition can be written as [21]

$$\sum_{\mathrm{em., abs.,} e-e} \sum_f \sum_i \frac{n_i}{\tau_{\mathrm{if}}} (E_i - E_f + \delta E) = 0 \qquad (3)$$

where $E_i - E_f$ is the subband separation, and the change in energy δE is equal to $-E_{\mathrm{LO}}$ for phonon emission (em.), $+E_{\mathrm{LO}}$ for absorption (abs.) and zero for electron–electron (e-e) scattering. The next step of the procedure, is to vary the electron temperature until (3) is satisfied self-consistently.

From the self-consistent solution, the population inversion $\Delta n_i = n_9 - n_7$ in the steady-state condition is obtained and the modal gain can be calculated [2], [20]

$$G_M = \frac{4\pi e^2}{\epsilon_0 \underline{n}} \frac{z_{97}^2}{2\gamma_{97} L_p \lambda} \Gamma(n_9 - n_7) \qquad (4)$$

where λ is the laser emission wavelength, $2\gamma_{97}$ is the experimental full-width at half maximum (FWHM) of the electroluminescence spectrum below threshold, $\underline{n}$ is the mode refractive
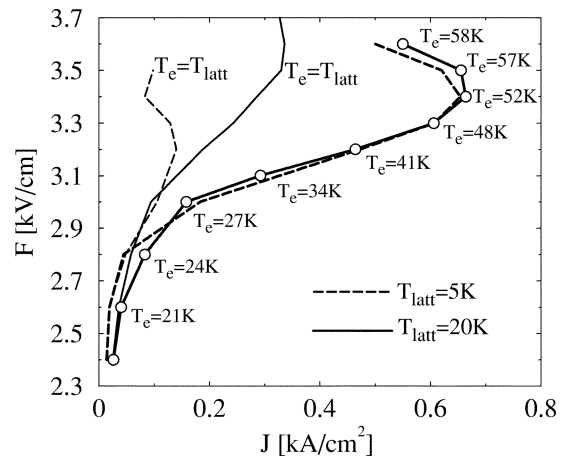

Fig. 2. Electric field versus current density characteristics at lattice temperature $T_{\mathrm{latt}} = 5$ K and $T_{\mathrm{latt}} = 20$ K.

index, ϵ_0 is the vacuum dielectric permittivity, L_p is the length of one period (injector + active region), Γ is the modal overlap factor, and z_{97} is the radiative transition matrix element. To extract the output characteristics of QCLs, one has to change the electric field F (i.e., the applied voltage) and calculate the modal gain G_M and the total current density J for each value of the field. The threshold current density J_{th} is found according to $G_M(J_{\mathrm{th}}) = \alpha_M + \alpha_W$, where α_M and α_W are the mirror and waveguide losses, respectively.

Fig. 2 shows the calculated electric field-current density characteristics at lattice temperatures of $T_{\mathrm{latt}} = 5$ K and 20 K for the terahertz QCL [14], with the electron temperature assumed equal to that of the lattice ($T_e = T_{\mathrm{latt}}$; (2) and (1) only), and, on the other hand, using the full-model calculation with the kinetic energy balance equation included (3). Under the assumption $T_e = T_{\mathrm{latt}}$, the $F - J$ curves show current density saturation and negative differential resistance (NDR) features at very low currents; i.e., $\sim$150 A/cm^2 at 5 K, and $\sim$350 A/cm^2 at 20 K, which are not consistent with experimental results [13], [14]. Instead, measurements show only a small sensitivity of $F - J$ on lattice temperature, which we indeed find with the full calculation, which includes the energy balance. The current is predicted to saturate at $\sim$680 A/cm^2 in reasonable agreement with that measured at $\sim$820 A/cm^2 [13], [14]. The discrepancy of about 20% is probably related to the fact that we have restricted consideration to a 13-level system, i.e., the parasitic leakage currents from the injector to higher states are neglected. For example, those could be up to 30% of total current density under the higher field/higher current operating conditions in mid-infrared QCLs [22]. The average electron temperature are also shown in Fig. 2. T_e increases from the lattice temperature, under very low injection, up to $\sim$60 K when the NDR occurs. The electron temperatures are more sensitive to the current density than in mid-infrared devices [21]. This is due to the fact that electron–electron scattering is by far the fastest scattering mechanism in terahertz QCLs, with their relatively small spacing between states. Therefore, the inelastic electron-LO phonon scatterings, which couples electron distributions to the lattice heath bath, does not manage to cool electrons as efficiently as in mid-infrared devices. The calculations

REFERENCES

[1] J. Faist, F. Capasso, D. L. Sivco, C. Sirtori, A. L. Hutchison, and A. Y. Cho, "Quantum cascade laser," *Science*, vol. 264, pp. 553–556, 1994.
[2] C. Gmachl, F. Capasso, D. L. Sivco, and A. Y. Cho, "Recent progress in quantum cascade lasers and applications," *Rep. Prog. Phys.*, vol. 64, pp. 1533–1601, 2001.
[3] C. Gmachl, D. L. Sivco, R. Colombelli, F. Capasso, and A. Y. Cho, "Ultra-broadbend semiconductor laser," *Nature*, vol. 415, pp. 883–887, 2002.
[4] C. Sirtori, H. Page, C. Becker, and V. Ortiz, "GaAs-AlGaAs quantum cascade lasers: Physics, technology, and prospects," *IEEE J. Quantum Electron.*, vol. 38, pp. 547–558, June 2002.
[5] K. Faist, D. Hofstetter, M. Beck, T. Aellen, M. Rochat, and S. Blaser, "Bound-to-continuum and two-phonon resonance quantum-cascade lasers for high duty cycle, high-temperature operation," *IEEE. J. Quantum Electron.*, vol. 38, pp. 533–546, June 2002.
[6] J. Ulrich, J. Kreuter, W. Schrenk, G. Strasser, and K. Unterrainer, "Long wavelength (15 and 23 μm) GaAs/AlGaAs quantum cascade lasers," *Appl. Phys. Lett.*, vol. 80, pp. 3691–3693, 2002.
[7] K. Unterrainer, R. Colombelli, C. Gmachl, F. Capasso, H. Y. Hwang, A. M. Sergent, D. L. Sivco, and A. Y. Cho, "Quantum cascade lasers with double metal-semiconductor waveguide resonators," *Appl. Phys. Lett.*, vol. 80, pp. 3060–3062, 2002.
[8] R. Colombelli, F. Capasso, C. Gmachl, A. L. Hutchinson, D. L. Sivco, A. Tredicucci, M. C. Wanke, A. M. Sergent, and A. Y. Cho, "Far-infrared surface-plasmon quantum-cascade lasers at 21.5 and 24 μm wavelengths," *Appl. Phys. Lett.*, vol. 78, pp. 2120–2622, 2001.
[9] M. Rochat, J. Faist, M. Beck, U. Oesterle, and M. Ilegems, "Far-infrared ($\lambda = 88$ μm) electroluminescence in quantum cascade structure," *Appl. Phys. Lett.*, vol. 73, pp. 3724–3726, 1998.
[10] R. Colombelli, A. Straub, F. Capasso, C. Gmachl, M. I. Blakey, A. M. Sergent, S. N. G. Chu, K. W. West, and L. N. Pfeiffer, "Terahertz electroluminescence from superlattice quantum cascade structure," *J. Appl. Phys.*, vol. 91, pp. 3526–3529, 2002.
[11] P. Harrison and R. A. Soref, "Population-inversion and gain estimates for a semiconductor TASER," *IEEE J. Quantum Electron.*, vol. 37, pp. 153–158, Jan. 2001.
[12] R. Köhler, R. C. Iotti, A. Tredicucci, and F. Rossi, "Design and simulation of terahertz quantum cascade lasers," *Appl. Phys. Lett.*, vol. 79, pp. 3920–3922, 2001.
[13] R. Köhler, A. Tredicucci, F. Beltram, H. E. Beere, E. H. Linfield, A. G. Davies, and D. A. Ritchie, "High-intensity interminiband terahertz emission from chirped superlattice," *Appl. Phys. Lett.*, vol. 80, pp. 1867–1869, 2002.
[14] R. Köhler, A. Tredicucci, F. Beltram, H. E. Beere, E. H. Linfield, A. G. Davies, D. A. Ritchie, R. C. Iotti, and F. Rossi, "Terahertz semiconductor-heterostructure laser," *Nature*, vol. 417, pp. 156–159, 2002.
[15] M. Rochat, L. Ajili, H. Willenberg, J. Faist, H. E. Beere, A. G. Davies, E. H. Linfield, and D. A. Ritchie, "Low-threshold terahertz quantum cascade lasers," *Appl. Phys. Lett.*, vol. 81, pp. 1381–1383, 2002.
[16] R. C. Iotti and F. Rossi, "Nature of charge transport in quantum-cascade lasers," *Phys. Rev. Lett.*, vol. 87, pp. 146603-1–146603-4, 2001.
[17] P. Harrison, *Quantum Wells, Wires and Dots: Theoretical and Computational Physics*. Chichester, U. K.: Wiley, 1999.
[18] ——, "The nature of the electron distribution function in quantum cascade lasers," *Appl. Phys. Lett.*, vol. 75, pp. 2800–2802, 1999.
[19] K. Donovan, P. Harrison, and R. W. Kelsall, "Self-consistent solution to the intersubband rate equations in quantum cascade lasers: Analysis of a GaAs/AlxGa$1 - x$As device," *J. Appl. Phys.*, vol. 89, pp. 3084–3090, 2001.
[20] D. Indjin, P. Harrison, R. W. Kelsall, and Z. Ikonić, "Self-consistent scattering theory of transport and output characteristics of quantum cascade lasers," *J. Appl. Phys.*, vol. 91, pp. 9019–9026, 2002.
[21] P. Harrison, D. Indjin, and R. W. Kelsall, "The electron temperature and mechanisms of hot carrier generation in quantum cascade lasers," *J. Appl. Phys.*, vol. 92, pp. 6921–6923, 2002.
[22] D. Indjin, P. Harrison, R. W. Kelsall, and Z. Ikonić, "Influence of leakage current on temperature performance of GaAs/AlGaAs quantum cascade lasers," *Appl. Phys. Lett.*, vol. 81, pp. 400–402, 2002.
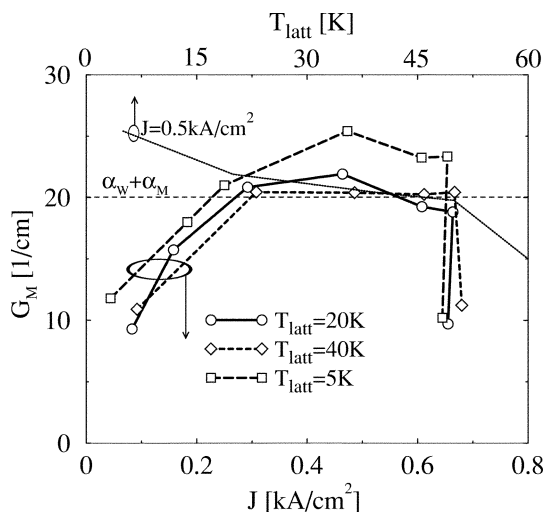

Fig. 3. Calculated modal gain versus current density dependence at cryogenic temperatures (bottom axis) and modal gain versus lattice temperature dependence for specific near optimal current density of $J = 500$ A/cm^2 (top axis). The horizontal dashed line denotes the total losses ($\alpha_M + \alpha_W \approx 20$ cm^{-1}) [14].

also show that T_e has a prominent second-order dependence on current density, and can be written (up to the NDR feature) as $T_e \approx T_{latt} + \alpha_1 J + \alpha_2 J^2$, where $\alpha_1 \sim 27$ K/(kAcm^{-2}), and $\alpha_2 \sim 35$ K/(kAcm^{-2})^2.

In Fig. 3 the modal gain versus current density dependence (bottom axis) at lattice temperatures of 5 K, 20 K, and 40 K is calculated with $\lambda = 70$ μm, $\underline{n} = 3.28, \Gamma = 0.47, L_p = 104.9$ nm, and $2\gamma_{97} = 2$–2.2 meV [13]. In accordance with the experimentally obtained losses [14] from the intersection points of the total loss line $\alpha_M + \alpha_W \approx 20$ cm^{-1} and the $G_M(J)$ lines, we obtain threshold currents $J_{th} = 250$–300 A/cm^2, in good agreement with experiment [14]. The structure starts to loose optical power quite abruptly at about $\sim$650 A/cm^2, also in accordance with experimental findings, i.e., close to the saturation of the injected (nonparasitic) current. The modal gain versus lattice temperature for a near optimal current density $J = 500$ A/cm^2 is also given in Fig. 3 (top axis). The model predicted that the laser is able to run up to $\sim$50 K which is close to the experimental maximum of $\sim$55 K [14].

In summary, we have used a fully self-consistent rate equation method for modeling carrier dynamics in terahertz QCLs. The results from the model are in very good agreement with experimental data. The calculations show large sensitivity of the electron temperature to the injection current, a fact that must be controlled through improved/optimized structure design to achieve high temperature operation of terahertz lasers.